

## Quantitative imaging and correction for cascade gamma radiation of $^{76}\text{Br}$ with 2D and 3D PET

Mark Lubberink<sup>1,2</sup>, Harald Schneider<sup>2</sup>, Mats Bergström<sup>2</sup> and Hans Lundqvist<sup>1</sup>

<sup>1</sup> Section of Biomedical Radiation Sciences, Rudbeck Laboratory, Uppsala University, 751 85 Uppsala, Sweden

<sup>2</sup> Uppsala Research Imaging Solutions AB/Uppsala University PET Centre, University Hospital, 751 85 Uppsala, Sweden

E-mail: mark.lubberink@pet.uu.se

Received 7 June 2002, in final form 30 July 2002

Published 18 September 2002

Online at [stacks.iop.org/PMB/47/3519](http://stacks.iop.org/PMB/47/3519)

### Abstract

Several positron emitting nuclides with applications in PET, such as  $^{76}\text{Br}$ ,  $^{124}\text{I}$ ,  $^{110\text{m}}\text{In}$  and  $^{86}\text{Y}$ , also emit gamma radiation in their decays. Measured coincidences between annihilation photons and this cascade gamma radiation are essentially true coincidences and the standard PET corrections do not account for them. We investigated the performance of  $^{76}\text{Br}$  in 2D and 3D PET, the effect of the gamma radiation emitted by  $^{76}\text{Br}$  on quantitative accuracy and the distribution of cascade gamma radiation coincidences in 2D and 3D PET sinograms. A correction method for cascade gamma radiation coincidences was implemented and evaluated. Count rate linearity was affected by the gamma radiation from the  $^{76}\text{Br}$  decay. Spatial resolution and sphere recovery were slightly worse for  $^{76}\text{Br}$  compared to  $^{18}\text{F}$ . Correction for cascade gamma radiation coincidences by subtraction of a linear projection tail fit improved total correction accuracy to similar values as for positron-only emitters such as  $^{18}\text{F}$ , and improved image contrast significantly.

### 1. Introduction

A number of positron emitters besides the commonly used  $^{18}\text{F}$ ,  $^{11}\text{C}$ ,  $^{15}\text{O}$ ,  $^{15}\text{N}$  or  $^{82}\text{Rb}$  have in recent years found an application in PET.  $^{76}\text{Br}$  was used in studies of monoclonal antibody kinetics (Lövqvist *et al* 1999), which requires a radionuclide with a longer half-life than the standard PET nuclides, and in brain studies (Ribeiro *et al* 1999).  $^{124}\text{I}$  (Pentlow *et al* 1991) and  $^{66}\text{Ga}$  (Graham *et al* 1997) were used for similar purposes. Positron emitting analogues of therapeutic nuclides, such as  $^{86}\text{Y}$  (Herzog *et al* 1993),  $^{110\text{m}}\text{In}$  (Lubberink *et al* 2002),  $^{83}\text{Sr}$  (Lundqvist *et al* 1999, Rösch *et al* 1996) and also  $^{124}\text{I}$  (Flower *et al* 1994) have been suggested for improved dosimetry of radionuclide therapy with  $^{90}\text{Y}$ ,  $^{111}\text{In}$ ,  $^{89}\text{Sr}$  and  $^{131}\text{I}$ , respectively.

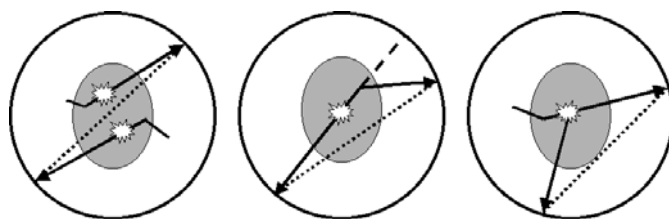


Figure 1. From left to right: random coincidences, coincidences of scattered photons and coincidences involving cascade gamma radiation.

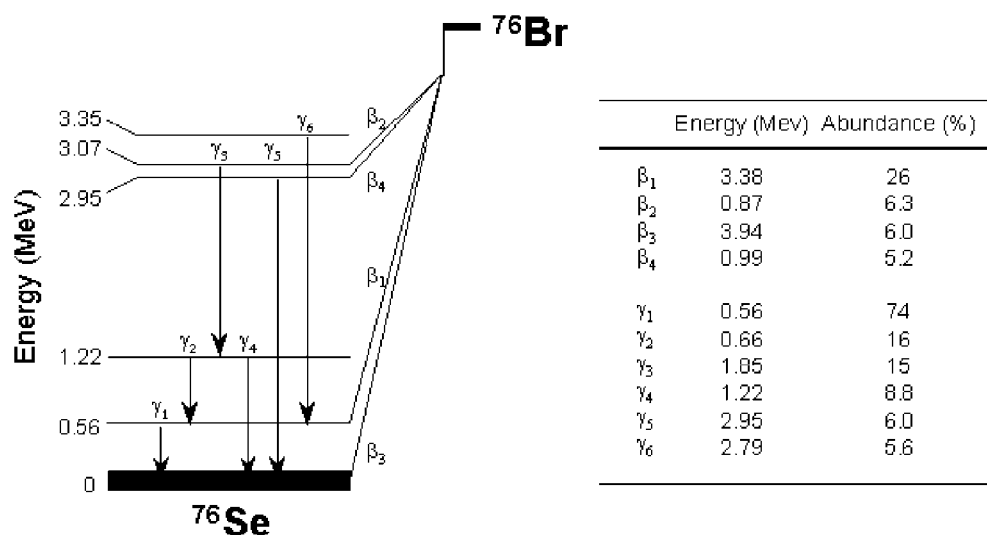


Figure 2. Simplified decay scheme of  $^{76}\text{Br}$  ( $t_{1/2} = 16.2$  h), showing positrons and gamma radiation with abundances over 5%. From Löqvist *et al* (1999), with data from Chu *et al* (1999).

The iron isotope  $^{52}\text{Fe}$  has been used in, for example, studies of anaemia (Beshara *et al* 1999). Several copper isotopes, among them  $^{60}\text{Cu}$  (Martin *et al* 1995), have also been suggested for use with PET.

All of these nuclides emit gamma radiation in cascade with positrons. Detection of essentially true coincidences of these gamma with each other or with annihilation photons introduces a bias in the images which is not corrected for by the standard PET corrections (Martin *et al* 1995, Kohlmyer *et al* 1999, Lubberink *et al* 1999, Pentlow *et al* 2000, Herzog *et al* 2002), see also figure 1. This effect is probably largest for  $^{86}\text{Y}$ ,  $^{76}\text{Br}$ ,  $^{52\text{m}}\text{Mn}$  and  $^{110\text{m}}\text{In}$ . These nuclides emit a large amount of gamma radiation with energies over 300 keV, 309%, 198%, 100% and 98% per decay, respectively, compared to 33%, 54%, 97% and 62% positrons. In 26% of all  $^{76}\text{Br}$  decays a positron is emitted simultaneously with one 559 keV gamma, and in 22% of the decays a positron is emitted in cascade with more than one gamma among which in most cases the same 559 keV gamma, a 657 keV gamma or a 563 keV gamma (figure 2). High-energy gamma emitted by  $^{76}\text{Br}$  or  $^{86}\text{Y}$  can also give pair production (Kohlmyer *et al* 1999) but this has a low probability. Apart from an increased image background, the increased singles rate due to the gamma radiation may also lead to inaccurate dead time correction (Martin *et al* 1995).

Recently, two other publications compared PET with  $^{18}\text{F}$  and  $^{76}\text{Br}$ , mainly focusing on the higher positron energies and resulting degradation of resolution (Löqvist *et al* 1999,

Ribeiro *et al* 1999). The observed loss of contrast for  $^{76}\text{Br}$  compared to  $^{18}\text{F}$  was contributed to positron range (Ribeiro *et al* 2000). We previously reported results of 2D PET measurements with  $^{76}\text{Br}$  showing that the distribution of cascade gamma radiation coincidences is reasonably uniform (Lubberink *et al* 1999), and two other groups also suggested a correction for cascade gamma radiation from  $^{86}\text{Y}$  in 2D PET by subtraction of a uniform background (Pentlow *et al* 2000), a linear fit to the projection tails (Kohlmyer *et al* 1999) or a convolution subtraction technique (Beattie *et al* 2001). The aim of this work was to study the performance of 2D and 3D PET with  $^{76}\text{Br}$  and to implement and study the effects of a correction for cascade gamma coincidences. Measurements of correction accuracy, resolution, recovery, contrast, count rate performance, uniformity and influence of radioactivity outside the field of view (FOV) are presented.

## 2. Materials and methods

### 2.1. Tomographs

Measurements were made using an ECAT Exact HR+ (CTI/Siemens, Knoxville) tomograph (Adam *et al* 1997, Brix *et al* 1997) and in some cases also with a Scanditronix/GEMS 4096 + WB (Scanditronix AB, Uppsala, Sweden) tomograph (Rota Kops *et al* 1990). The HR+ system has retractable tungsten septa (thickness 0.8 mm, length 66.5 mm), whereas the 4096 has non-removable lead septa (thickness 3 mm, length 195 mm). These larger septa make the 4096 system much less sensitive to radiation reaching its detectors at oblique angles, and thus for scatter, randoms and gamma radiation. The measurements with the 4096 system will only be discussed when there is a considerable difference in methods or results compared to the HR+ measurements. Standard corrections for scattered radiation were used: convolution subtraction (Bergström *et al* 1983) in 2D mode for both scanners, and a simulation-based method for the HR+ in 3D mode (Watson *et al* 1997). Attenuation correction was either made analytically or based on a transmission scan.

### 2.2. Correction for cascade gamma radiation coincidences

The aim of a cascade gamma coincidence correction is to subtract all cascade gamma coincidences, in order to provide a 'proper' sinogram for further corrections and reconstruction. An important advantage of this approach, as opposed to including correction for cascade gamma coincidences in a scatter correction, is that no nuclide-specific corrections are required. Two methods have been suggested: projection tail fit subtraction method, using either a linear fit (Kohlmyer *et al* 1999) or a uniform background (Lubberink *et al* 1999, Pentlow *et al* 2000) or a convolution subtraction correction (Beattie *et al* 2001). These methods were suggested for General Electric Advance and 4096 WB scanners (General Electric Medical Systems, Milwaukee) in 2D mode.

Here, we implemented a correction that subtracts all counts under a linear fit between the outermost elements at each projection tail of the uncorrected projections. Based on the fact that the outermost HR+ projection elements are not zero even for  $^{18}\text{F}$ , as seen in the phantom measurements in the next paragraph, the cascade gamma coincidence background in the outermost projection elements was assumed to be 80% of the measured counts in 3D mode, and 90% in 2D mode. In short, the five outermost projection elements at both tails are multiplied by 0.8 (3D) or 0.9 (2D), and the cascade gamma contribution is determined by a linear fit to these outermost projection elements. Subsequently, all counts under this linear fit

are subtracted from the projection. In the case of the 4096 scanner, all counts in the outermost projection elements were assumed to be cascade gamma radiation coincidences.

### 2.3. Scatter, attenuation and cascade gamma correction accuracy

The NEMA phantom (Karp *et al* 1991) was filled with approximately 40 MBq of  $^{76}\text{Br}$  or  $^{18}\text{F}$  and placed centrally in the FOV. This 20 cm diameter, 18.5 cm long fillable cylinder contains cold 5 cm diameter cylindrical water, air and Teflon inserts positioned at 6 cm from the phantom axis in  $120^\circ$  increments. A series of six 10 min emission scans was made both in 2D and in 3D acquisition mode, followed by a 10 min hot (i.e. in the presence of radioactivity in the phantom) transmission scan. The 4096 hot transmission scan was corrected for emission counts by subtraction of a short emission scan. Approximately 20 h after the  $^{18}\text{F}$  measurement a second, cold (i.e. without radioactivity in the phantom), transmission scan was made to assess the effect of the radioactivity in the phantom on correction accuracy. Images were reconstructed using the standard corrections, including scatter and attenuation correction, and cascade gamma correction. The correction error in each insert was determined by dividing the measured radioactivity concentration in a 3 cm diameter volume of interest (VOI) in that insert by the radioactivity concentration in four similar VOIs in the radioactive solution.

To calculate the relative number of cascade gamma coincidences, the  $^{18}\text{F}$  projections were scaled by the total counts inside the phantom relative to the total counts inside the  $^{76}\text{Br}$  phantom, determined by subtraction of a background calculated by linear interpolation of projection elements just outside the phantom. The number of cascade gamma coincidences in the scaled  $^{76}\text{Br}$  sinogram was determined by subtraction of a scaled  $^{18}\text{F}$  sinogram from the  $^{76}\text{Br}$  sinogram.

### 2.4. Spatial resolution

Transaxial resolution was measured using a 1 mm inner diameter catheter crossing a  $5 \times 20 \times 45$  cm polyethylene block, placed centrally in the FOV of the camera, at 0, 5, 10 and 20 cm from the centre of the block. The catheter was filled with 10–20 MBq of  $^{76}\text{Br}$  or  $^{18}\text{F}$  and a 15 min emission scan was made. Attenuation correction was based on a 10 min cold transmission scan. Images were reconstructed with a pixel size of 1.03 mm (HR+) or 2 mm (4096). Spatial resolution, as full width at half maximum (FWHM) and tenth maximum (FWTM) of the point spread function, was calculated by linear interpolation between points in a horizontal and vertical profile through the peak maximum.

### 2.5. Recovery

A phantom containing spheres with diameters ranging from 10 mm to 38 mm was filled with water. To ensure a similar radioactivity concentration in each sphere, approximately 50 MBq of  $^{76}\text{Br}$  or  $^{18}\text{F}$  was diluted in 100 ml water and all spheres were filled from this solution. Fifteen-minute 2D and 3D emission scans were made, on the HR+ acquiring approximately 20 million (2D) or 100 million (3D) gross trues per slice in the slices containing the spheres. For the 4096 scanner, on which the phantom can be mounted in a fixed position, a cold transmission scan was done before the start of the measurement. For the HR+, analytical attenuation correction based on a definition of an ellipse was applied. This gives a small error because of the presence of the patient bed, but attenuation correction based on a hot transmission scan leads to severe image artefacts in this case. Images were reconstructed to a pixel size of 1.03 mm (HR+) or 1 mm (4096). Hot-spot recovery coefficients (HSR) for

each sphere were calculated by dividing the radioactivity concentration in a region of interest (ROI) with the same diameter as the spatial resolution in that sphere by the radioactivity concentration in a similar ROI in the largest sphere. This is a somewhat simplified procedure compared to the IEC guidelines (Adam *et al* 1997). Alternatively, 1 cm diameter ROIs and half-maximum ROIs, drawn at 50% of the maximum radioactivity concentration, were used. The area of these last ROIs was compared to the true sphere size to assess the accuracy of size prediction using a half-maximum ROI.

In a measurement with the same phantom, the spheres were filled with cold water and the rest of the phantom with circa 40 MBq of  $^{76}\text{Br}$  or  $^{18}\text{F}$ . This measurement was not done on the 4096 system. Emission scans in 2D and 3D modes were made, acquiring  $2 \times 10^9$  gross trues to ensure similar image statistics as in the hot spot recovery measurements, and in the reconstruction analytical attenuation correction and cascade gamma coincidence corrections were applied. Again, analytical attenuation correction leads to a small error because of the presence of the patient bed, but a hot transmission could not be used because the spheres were clearly visible in the attenuation image, even after segmentation using the method included in the HR+ software. Images were reconstructed to a pixel size of 1.03 mm. Cold-spot recovery coefficients (CSR) were calculated by division of the mean of the measured radioactivity concentrations in spatial resolution sized ROIs in three image planes through each sphere by the mean of the radioactivity concentration measured in 15 cm diameter ROIs in five image planes not containing the spheres.

## 2.6. Contrast

The effect of cascade gamma coincidence correction on image contrast was evaluated assuming that the measured radioactivity concentration in a sphere is determined by the following equation:

$$A_{s,m} = \text{HSR} \cdot A_{s,t} + \text{CSR} \cdot A_{b,m} \quad (1)$$

where  $A$  is radioactivity concentration and the indices  $s, b, t$  and  $m$  indicate sphere, background, true and measured. HSR and CSR are hot-spot and cold-spot recovery coefficients. This is based on a linear system performance, which assumes accurate attenuation and scatter correction (Geworski *et al* 2000). Measured sphere-to-background ratio ( $A_{s,m}/A_{b,m}$ ) as a function of the actual radioactivity concentration ratio  $A_{s,t}/A_{b,t}$  in each sphere is then, assuming that all data are properly corrected, calculated as

$$\frac{A_{s,m}}{A_{b,m}} = \frac{1}{g} \cdot \text{HSR} \cdot \frac{A_{s,t}}{A_{b,t}} + \text{CSR}. \quad (2)$$

This value can also be seen as a measure of contrast. The factor  $g$  indicates the over-estimation of measured radioactivity caused by cascade gamma radiation coincidences. This factor was determined by division of the mean radioactivity concentration in a 15 cm diameter VOI in five slices, not containing the spheres, in an image that was not corrected for cascade gamma radiation by the same concentration in a cascade gamma-corrected image. Measured sphere-to-background ratio, or image contrast, as a function of true radioactivity concentration ratio, with and without cascade gamma coincidence correction, was calculated using the equation above for spheres of various sizes and true relative uptakes of 2, 4, 8.

For comparison with measured data, the spheres in the sphere phantom were filled with 5 kBq ml $^{-1}$  of  $^{76}\text{Br}$  and the rest of the phantom with 0.75 kBq ml $^{-1}$  of the same nuclide. The phantom was placed centrally in the FOV and a 15 min emission scan was made both in 2D and 3D modes. Images were reconstructed using the standard corrections, including scatter correction and analytical attenuation correction, and linear tail fit background subtraction to

correct for cascade gamma coincidences. The measured radioactivity concentrations in a spatial resolution size ROI in each sphere and the measured radioactivity in a 15 cm diameter VOI in five planes not containing the spheres were used to calculate image contrast.

## 2.7. Count rate characteristics

**2.7.1. Count rate linearity.** A 20 cm diameter cylindrical phantom was filled with circa 150 MBq of  $^{76}\text{Br}$  or  $^{11}\text{C}$  and placed centrally in the FOV of the scanner. Subsequent emission scans were made in 2D and 3D modes during 4 days and 3 h, respectively. After image reconstruction applying standard corrections, measured radioactivity concentration in a 15 cm diameter VOI in all image planes was plotted versus the true phantom radioactivity concentration.

**2.7.2. Noise equivalent count rates.** NEC rates (Strother *et al* 1990) were calculated using the following equation, adapted for gamma radiation emitting nuclides:

$$\text{NEC} = \frac{T^2}{T + fG + S + 2fD} \quad (3)$$

where  $T$  is the scatter and cascade gamma corrected trues count rate,  $S$  is the scatter count rate calculated as the NEMA scatter fraction (Brix *et al* 1997) multiplied with the cascade gamma corrected gross trues count rate,  $G$  the cascade gamma radiation coincidences count rate, assumed to be 32% of the gross trues count rate in 2D and 45% in 3D based on the NEMA phantom measurements above,  $f$  the average fraction of the projection taken up by the object and  $D$  the delayed coincidence, or random, count rate.

## 2.8. Uniformity

Uniformity was only measured for the HR+ scanner. A uniformly filled 20 cm diameter phantom was placed in the centre of the scanner and filled with approximately 40 MBq of  $^{76}\text{Br}$  or  $^{18}\text{F}$ . Emission scans were made until 100 million true counts were acquired for  $^{18}\text{F}$  or 100, 145 or 185 million counts for  $^{76}\text{Br}$ , either neglecting cascade gamma coincidences or considering a relative amount of cascade gamma coincidences of 32% (2D) or 45% (3D). This procedure was repeated for a standard torso phantom (width 30 cm, height 23 cm; as in NEMA NU2-2001, Performance measurements of positron emission tomographs). This torso phantom was positioned on the patient bed, covering the whole axial FOV, with its widest point in the vertical centre of the FOV. The phantom contained approximately 50 MBq of either  $^{76}\text{Br}$  or  $^{18}\text{F}$  and 2D and 3D emission scans were done acquiring similar numbers of counts as for the cylindrical phantom. Emission measurements were followed by a 10 min transmission scan.

Images were reconstructed using the normal corrections, applying a 4 mm Hann filter and analytical attenuation correction for the cylindrical phantom and a 6 mm Gauss filter and segmented attenuation correction for the torso phantom, and the suggested cascade gamma coincidence correction. A total of 33 or 39  $2 \times 2$  cm square ROIs were drawn in each slice in the cylinder and torso phantom image, respectively, and maximum and minimum volume non-uniformities (NU+ and NU-) were calculated as described previously (Karp *et al* 1991). One  $22 \times 15$  cm ellipse-shaped ROI was drawn in each slice in the torso phantom images and one 15 cm diameter ROI was drawn in each cylinder phantom slice, and the slice non-uniformities and the standard deviation of the mean radioactivity concentration in the VOI combining all these ROIs were calculated.

**Table 1.** Scatter and attenuation correction errors (%) in water, air and Teflon

	$^{18}\text{F}$ , HR + 2D	$^{76}\text{Br}$ , HR + 2D	$^{18}\text{F}$ , HR + 3D	$^{76}\text{Br}$ , HR + 3D	$^{18}\text{F}$ , 4096	$^{76}\text{Br}$ , 4096
Water	7.7	16.6	7.7	26.9	1.6	5.1
Air	10.0	6.7	1.5	-3.8	8.1	7.5
Teflon	8.6	27.9	16.2	55.8	-2.7	5.0

**Table 2.** Residual correction errors (%) for  $^{76}\text{Br}$  in water, air and Teflon, after linear tail fit cascade gamma coincidence correction

	HR + 2D	HR + 3D	4096
Water	8.3	8.1	0.9
Air	11.2	2.7	9.0
Teflon	10.0	14.9	-5.8

### 2.9. Radioactivity outside the FOV

The NEMA phantom containing only the cold water insert was filled with circa 40 MBq of  $^{76}\text{Br}$  or  $^{18}\text{F}$  and placed central in the FOV on the patient bed of the HR+. A 1 ml source with 0.5 cm thick plexiglass walls, also containing approximately 40 MBq of  $^{76}\text{Br}$  or  $^{18}\text{F}$ , was positioned at 10 cm from the phantom outside the FOV on the camera axis. Emission scans (10 min) were made both with and without the external source. ROIs (3 cm diameter) were drawn in the radioactive solution and in the insert in the NEMA phantom, and the measured radioactivity concentrations with and without the external phantom were compared. In a second measurement, the same 1 ml source, containing approximately 40 MBq of  $^{76}\text{Br}$  or  $^{18}\text{F}$ , was placed on the patient bed at 50 cm from the axial FOV and step-wise moved towards the centre of the axial FOV. At each position a 2 min emission scan was done. This was repeated with and without the neuro-insert in place, a lead side shield ring that can be inserted at the entrance of the FOV.

## 3. Results

### 3.1. Scatter, attenuation and cascade gamma correction accuracy

Total correction accuracy is given in tables 1 and 2. Summation of all six frames before cascade gamma correction and reconstruction did not lead to significantly smaller correction errors. A 1 h transmission measurement, and even a 10 min transmission measurement with new rod sources, performed at a later time, lead to much improved values for  $^{76}\text{Br}$ , indicating that the relatively large correction errors in table 2 are mainly the sum of a cascade gamma coincidence contribution and attenuation correction errors caused by a low transmission pin source activity at the time of the measurements. The correction accuracy results are not consistent with the results published by Brix *et al* (1997), which gave correction errors in water of approximately 0% for  $^{18}\text{F}$  in both 2D and 3D modes with this phantom positioned 2.5 cm off-centre.

The relative number of cascade gamma coincidence was found to be 45% in 3D mode and 32% in 2D mode for the HR+ scanner. In a similar measurement with the 4096, the cascade gamma fraction was 12%. Figure 3 shows measured projections.

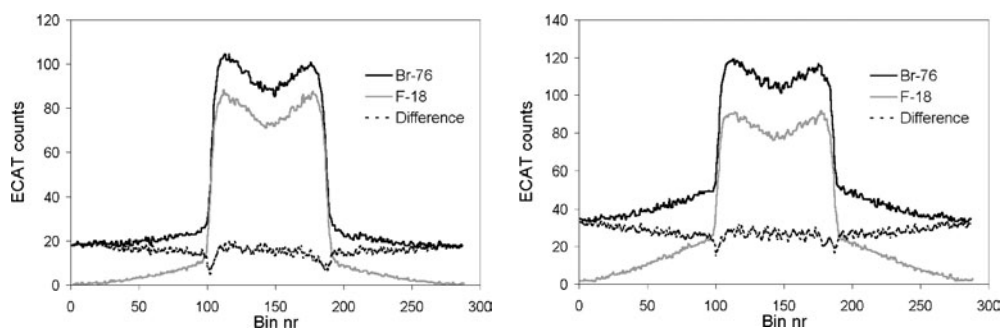


**Figure 3.** Measured profiles of a uniform cylinder in 2D (left) and 3D modes (right) for  $^{76}\text{Br}$  and  $^{18}\text{F}$ . Note that the projection tails are not zero even for  $^{18}\text{F}$ .

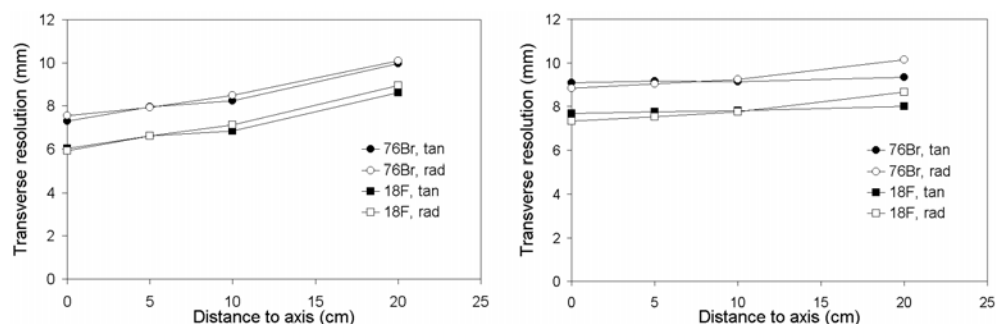


**Figure 4.** Transverse resolution, FWHM, in polyethylene for  $^{76}\text{Br}$  and  $^{18}\text{F}$ , using a 4 mm Hann filter, for the HR+ (left) and 4096 (right). Central FWTM values were 16.2 and 11.4 mm for the HR+ and 18.1 and 14.2 mm for the 4096, respectively.

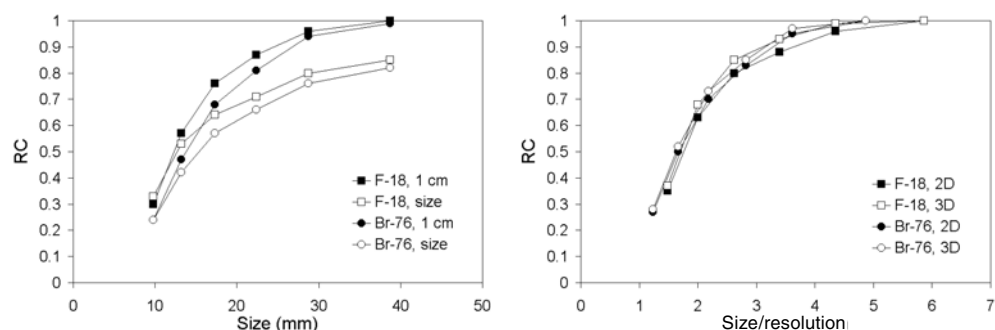
### 3.2. Spatial resolution

Figure 4 shows the spatial resolution in polyethylene. Central HR+ spatial resolution is 8.0 mm (FWTM 16.2 mm) for  $^{76}\text{Br}$ , compared to 6.0 mm (FWTM 11.4 mm) for  $^{18}\text{F}$ , using a 4 mm Hann filter. Using a similar filter, central transverse resolutions on the 4096 scanner were 9.0 and 7.5 mm for  $^{76}\text{Br}$  and  $^{18}\text{F}$ , respectively. For a 6 mm Gauss filter, used in HR+ whole body studies at our centre, the corresponding values were 9.5 and 8.0 mm.

### 3.3. Recovery

Hot-spot recovery coefficients are given in figure 5 and predicted sphere sizes using a half-maximum ROI in figure 6. Obviously  $^{76}\text{Br}$  recovery is worse than  $^{18}\text{F}$  recovery, although recovery measured using a resolution-sized ROI relative to sphere size is approximately similar. Maximum pixel recovery coefficients could also be used, but are usually very dependent on image statistics. Half-maximum ROIs estimate a sphere diameter that is slightly smaller than the true sphere diameter. Size estimation is as accurate for  $^{76}\text{Br}$  as for  $^{18}\text{F}$ .

Figure 7 shows cold-spot recovery and hot-spot recovery calculated using resolution size ROIs. Using hot-spot recovery coefficients divided by 1.08, to account for the residual correction error for radionuclides that do not emit gamma radiation (see table 1),  $1 - \text{HSR} / 1.08$  is equal to CSR in 2D mode for spheres larger than 1.5 cm, for  $^{18}\text{F}$  and also for  $^{76}\text{Br}$  after cascade gamma correction. The HR+ system is apparently not linear either for  $^{18}\text{F}$  or for  $^{76}\text{Br}$



**Figure 5.** Recovery coefficients (HR+) calculated using a 1 cm ROI and a half maximum ROI (left) and a resolution size ROI (right).

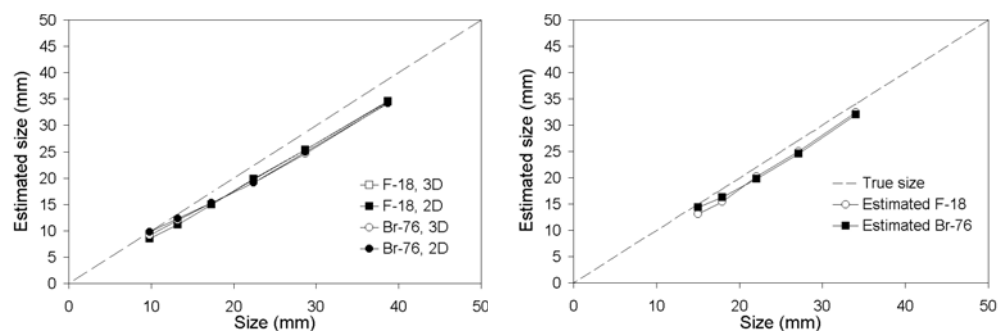


**Figure 6.** Predicted sphere size versus true sphere size using a half maximum ROI; HR+ (left) and 4096 (right).

in 3D mode, but cascade gamma correction does lead to similar results for  $^{76}\text{Br}$  as for  $^{18}\text{F}$  in the larger spheres.

### 3.4. Contrast

Figure 8 shows predicted and measured sphere-to-background ratios versus actual activity concentration ratios for spheres of different sizes. The predicted values were calculated using hot spot recovery coefficients divided by 1.08, as explained in the previous subsection. A gain in  $^{76}\text{Br}$  image contrast of up to 15% was obtained after correction for cascade gamma coincidences, resulting in a similar image contrast as for  $^{18}\text{F}$ . The measured data in figure 8 correspond well with the calculated data for the larger spheres (>2 cm), also in 3D mode where this method of contrast calculation is not accurate because of the nonlinearity of the system as shown in the recovery measurements. For the smallest spheres measured contrast is lower than expected from the calculated data. The poor image statistics of the measured data, which are closer to an actual clinical situation, probably lead to a degradation of contrast in the smaller spheres.

### 3.5. Count rate characteristics

The results of the count rate measurement are given in figures 9 and 10. Table 3 shows the corresponding values for the 50% dead time point, the peak NEC rate, and the points at which the gross (trues+scatter+gamma) and net trues rates equal the random rate. The  $^{76}\text{Br}$

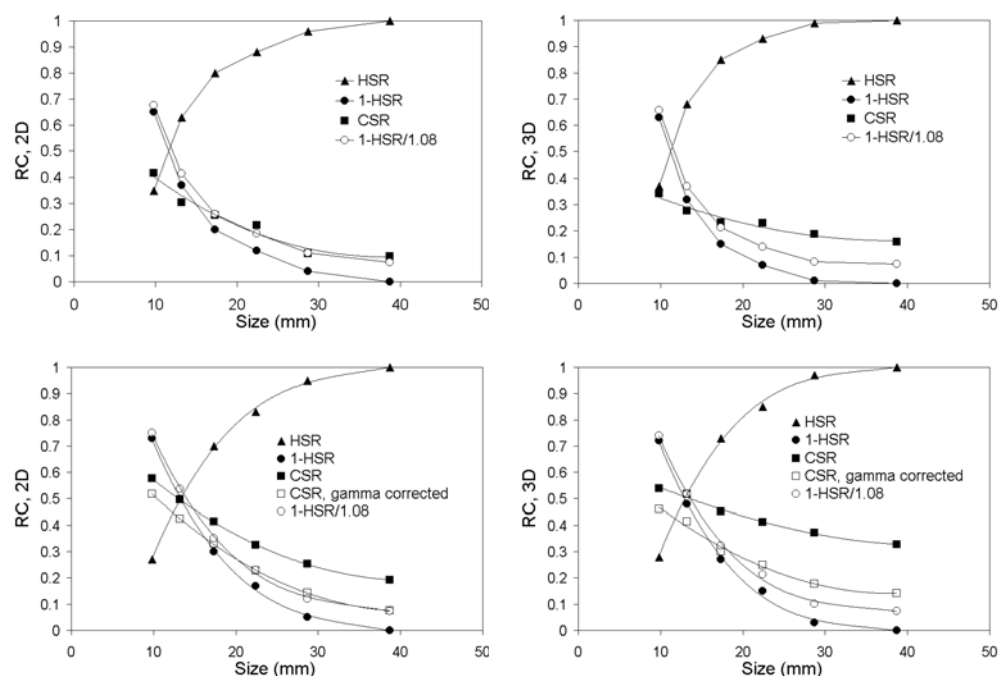


**Figure 7.** Hot spot (HSR) and cold spot (CSR) recovery coefficients, calculated using a spatial resolution size ROI, for  $^{18}\text{F}$  (top) and  $^{76}\text{Br}$  (bottom), in 2D (left) and 3D (right).

**Table 3.** Results of the HR+ count rate measurements

	50% DT	Peak NEC	$T + S(+G) = D$	$T = D$	$T = D_{\text{object}}$
$^{76}\text{Br}$ , 3D	450 kcps 16 kBq ml $^{-1}$	35 kcps 12 kBq ml $^{-1}$	340 kcps 9 kBq ml $^{-1}$	– –	140 kcps 10 kBq ml $^{-1}$
$^{76}\text{Br}$ , 2D	>65 kcps >19 kBq ml $^{-1}$	>14 kcps >19 kBq ml $^{-1}$	65 kcps 19 kBq ml $^{-1}$	23 kcps 10.5 kBq ml $^{-1}$	>65 kcps >19 kBq ml $^{-1}$

net true rate was less than the random rate at any activity concentration. The 3D net true rate is larger than the random rate inside the object for radioactivity concentrations below 10 kBq ml $^{-1}$ . Figure 10 shows that the HR+ dead time correction is not adequate for  $^{76}\text{Br}$ , whereas the 4096 dead time correction is correct.

### 3.6. Uniformity

Maximum and minimum non-uniformities are given in tables 4 and 5.

### 3.7. Radioactivity outside the FOV

Figure 11 shows the count rates resulting from a point source on the patient couch, at different distances to the axial FOV and with or without the neuro-insert in place. In figure 12, the radioactivity concentration measured in 3D mode in a cold water insert inside a  $^{76}\text{Br}$ -filled cylindrical phantom is shown both with and without the presence of a point source positioned

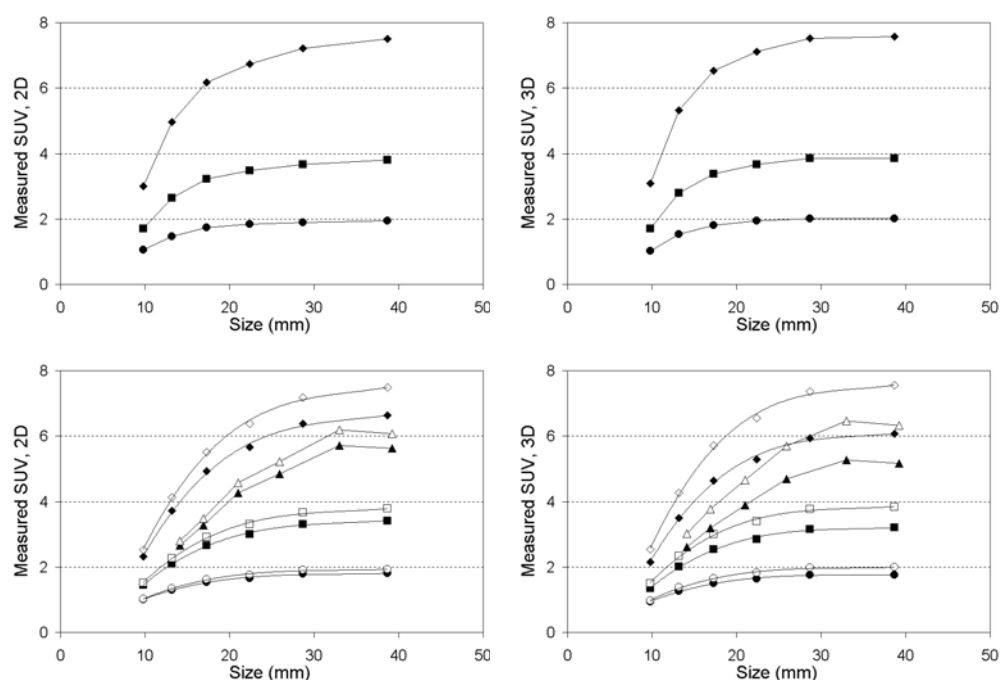


**Figure 8.** Measured and predicted sphere-to-background ratios versus sphere size for different actual uptake ratios (uptake ratios: diamonds 8, triangles 6.5 (measured), squares 4 and circles 2; open symbols corrected for cascade gamma coincidences). Top:  $^{18}\text{F}$ , bottom:  $^{76}\text{Br}$ , left: 2D, right: 3D.

10 cm outside the axial FOV. In 2D mode, there was no significant difference between the measured concentrations with and without external source.

#### 4. Discussion

We investigated the effect of  $^{76}\text{Br}$  positron energy on PET resolution and recovery and the effect on quantification of cascade gamma radiation coincidences in 2D and 3D PET with  $^{76}\text{Br}$ .

An initial degradation of quantitative accuracy of  $^{76}\text{Br}$  PET images compared to  $^{18}\text{F}$  was shown in the results above. The relative amount of  $^{76}\text{Br}$  cascade gamma coincidences was 45% in 3D mode and 32% in 2D mode, of which one-third inside the phantom resulting in a total phantom background of about 46% in 3D mode and 28% in 2D mode including the NEMA scatter fraction (Brix *et al* 1997). Instead of using  $fG + S$ , the NEMA scatter fraction could be measured specifically for  $^{76}\text{Br}$ . These values can be compared to  $^{86}\text{Y}$  NEMA scatter fractions of 25% in 2D and 67% in 3D for the GE Advance tomograph (Kohlmyer *et al* 1999). Application of a correction for cascade gamma radiation coincidences leads to residual correction errors of the same order as for  $^{18}\text{F}$ . Especially in 2D, nuclide-specific, spatially variant convolution subtraction scatter and cascade gamma correction is an option that may lead to better correction accuracy for more realistic radioactivity distributions than those studied here (Beattie *et al* 2001). This should be the subject of further investigations. In 3D, adaption of the HR+ model-based scatter correction (Watson *et al* 1997) to

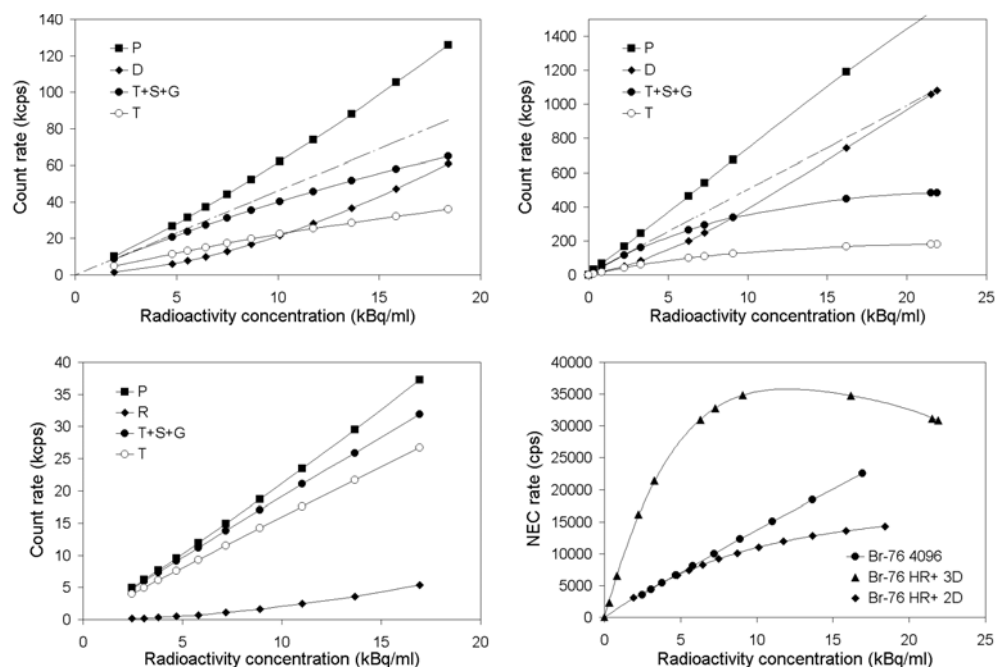


**Figure 9.** Top: HR+ prompt, delayed, gross and net trues count rates for  $^{76}\text{Br}$  in 2D mode (left) and 3D mode (right). The dashed lines are the trues rates extrapolated from low-activity data. Bottom: 4096 prompt, delayed, gross and net trues count rates for  $^{76}\text{Br}$  (left), and NEC rates (right).

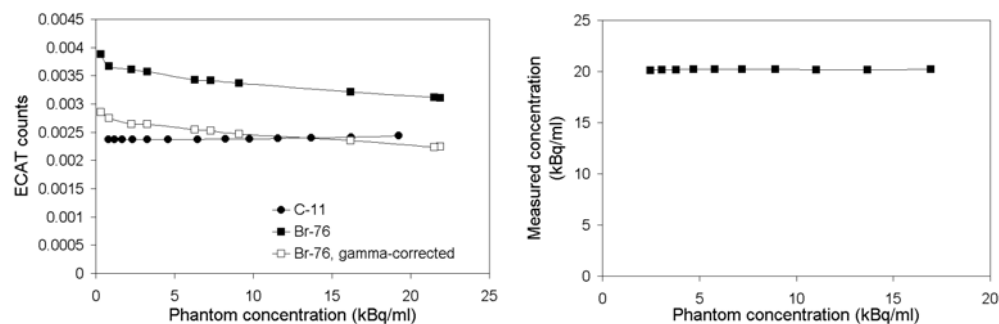


**Figure 10.** Counts per second per voxel after decay, dead time and abundance correction for the HR+ in 3D mode with  $^{11}\text{C}$  and  $^{76}\text{Br}$  (left), and measured radioactivity concentration for the 4096 with  $^{76}\text{Br}$  (right). HR+ results in 2D mode were similar to those in 3D mode.

gamma-emitting nuclides is also an option. The Gauss fit subtraction scatter correction on the GE Advance in 3D mode probably accounts for cascade gamma coincidences (Pentlow *et al* 2000).

The effect of cascade gamma radiation described here can be related to any cascade gamma radiation emitting nuclide, although the exact fraction of cascade gamma radiation coincidences depends on the relative number and energy of the emitted gamma, as well as the properties of the used tomograph.

Spatial resolution and recovery were found to be slightly worse for  $^{76}\text{Br}$  on both scanners, as previously reported in other publications (Löqvist *et al* 1999, Ribeiro *et al* 1999).

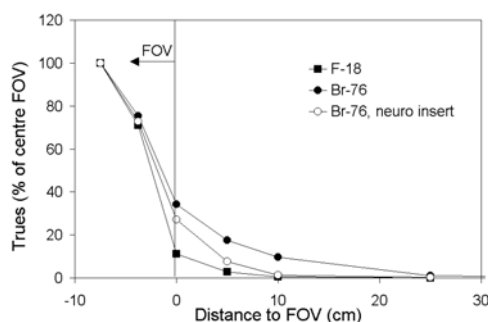


**Figure 11.** Gross trues count rates from a point source on the patient bed versus distance to the edge of the axial FOV, comparing  $^{76}\text{Br}$  and  $^{18}\text{F}$  without and with neuro-insert.

**Table 4.** Slice and volume uniformity (%) in a cylindrical phantom, for  $^{76}\text{Br}$  and  $^{18}\text{F}$ , HR+. LC = linear tail fit background subtraction.

	2D			3D		
	NU+	NU-	VOI SD/mean	NU+	NU-	VOI SD/mean
$^{18}\text{F}$ , slice	1.6	1.5		3.0	2.2	
$^{76}\text{Br}$ , slice	2.4	1.7		3.4	5.6	
$^{76}\text{Br}$ , slice, LC	2.5	2.4		4.0	4.5	
$^{18}\text{F}$ , volume	13	9	7	15	12	14
$^{76}\text{Br}$ , volume	14	13	10	23	19	24
$^{76}\text{Br}$ , volume, LC	12	12	10	17	19	24

**Table 5.** Slice and volume uniformity (%) in a torso phantom for  $^{76}\text{Br}$  and  $^{18}\text{F}$ . LC = linear background subtraction.

	NU+	NU-	VOI SD/mean
$^{18}\text{F}$ , slice	3.9	3.7	
$^{76}\text{Br}$ , slice	4.5	5.3	
$^{76}\text{Br}$ , slice, LC	6.3	4.2	
$^{18}\text{F}$ , volume	25	25	24
$^{76}\text{Br}$ , volume	32	25	30
$^{76}\text{Br}$ , volume, LC	37	44	35

However, contrast improves significantly after cascade gamma coincidence correction, and previously reported loss of contrast (Ribeiro *et al* 1999) for  $^{76}\text{Br}$  should thus rather be attributed to gamma radiation coincidences than to positron range.

The HR+ dead time correction is a quadratic fit of the total dead time to the singles count rate, determined by a decay measurement as that described here. For nuclides that emit only positrons, the singles-to-trues ratio is mainly depending on radioactivity concentration, and thus on the singles rate, which allows the dead time to be described as a function of singles count rate only. However, this ratio is different for cascade gamma radiation emitting nuclides, which results in an incorrect dead time prediction if the same function is used. Gamma that are rejected by the energy discriminator are not considered but do also contribute to

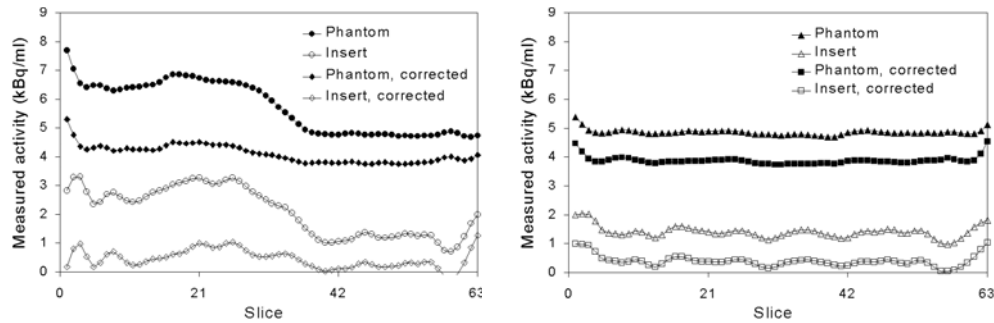


**Figure 12.** Measured radioactivity concentrations in a  $^{76}\text{Br}$ -filled cylindrical phantom with cold water insert in 3D mode, with (left) and without (right) a 40 MBq  $^{76}\text{Br}$ -point source at 10 cm from plane 63 outside the axial FOV, on the right-hand side of the figures. Data were corrected for cascade gamma radiation coincidences using a linear fit to the projection tails.

dead time. Specific dead time correction for  $^{76}\text{Br}$  can solve this problem. The dead time correction of the 4096 system is adequate for  $^{76}\text{Br}$  in the considered radioactivity interval. Dead time measurements were not done for very high radioactivity concentrations reaching the limits of the systems, but realistic radioactivity concentrations in patient studies with  $^{76}\text{Br}$  are of the order of a few  $\text{kBq ml}^{-1}$  to limit radiation dose to the patient, far below any saturation problems.

The increased influence of  $^{76}\text{Br}$  radioactivity outside of the FOV limits is applicability in 3D studies. The neuro-insert decreases this effect, but not quite to similar levels as obtained for  $^{18}\text{F}$  or  $^{11}\text{C}$  without a neuro-insert. Correction for gamma coincidences using the method described here leads to an improvement, but further investigation into the distribution of gamma radiation coincidences originating outside the FOV should be done.

Uniformity measurements showed that image noise is much increased for  $^{76}\text{Br}$  compared to  $^{18}\text{F}$  for images containing equal numbers of net true counts. This noise increase is relatively lower in 2D mode than in 3D mode. These results depend on the used radioactivity concentrations:  $^{76}\text{Br}$  concentrations relevant in clinical studies would lead to higher levels of image noise than for  $^{18}\text{F}$  even if similar numbers of net true counts were to be acquired in long measurements, because of the lower NEC rates at clinically relevant radioactivity concentrations. Random correction based on a delayed sinogram leads to an increase in image noise relative to random correction calculated from singles count rates (Strother *et al* 1990), which results in the factor 2 in the NEC equation (3). Because of the much higher random coincidence rates for  $^{76}\text{Br}$  compared to  $^{18}\text{F}$ , calculated random correction or smoothing of delayed projections before subtraction should be considered.

In conclusion, the main challenge to PET imaging with  $^{76}\text{Br}$ , causing degradation of quantitative accuracy and image contrast, is the cascade gamma radiation emitted in its decay. Specific dead time correction and cascade gamma coincidence correction improve quantitative accuracy, but more refined methods for description of the distribution of cascade gamma coincidences should be considered. The effect of increased levels of randoms could be improved by smoothing of the delayed sinograms before subtraction. On the other hand, the much lower NEC rate at clinically relevant radioactivity concentrations is a problem that cannot be evaded and leads to a degradation in quantitative accuracy and image quality in clinical studies, especially in 3D mode. The lower acceptance of cascade gamma coincidences and randoms due to thick, long septa and the linear count rate behaviour of the 4096 system seem to make this system as suitable for measurements of  $^{76}\text{Br}$  or other cascade gamma-emitting nuclides as modern systems with thin, short removable septa such as the HR+.

## Acknowledgments

The authors would like to thank Dr Vladimir Tolmachev, Dr Karl Johan Fasth and Dr Ulrika Yngve for production of  $^{76}\text{Br}$ , and the staff at Uppsala University PET Centre and Frank Janssen for help with measurements. Financial support was given by the Swedish Cancer Society, the Swedish Radiation Protection Agency and the Medical Faculty at Uppsala University.

## References

- Adam L E, Zaers J, Ostertag H, Trojan H, Bellemann M E and Brix G 1997 Performance evaluation of the whole-body PET scanner ECAT EXACT HR+ following the IEC standard *IEEE Trans. Nucl. Sci.* **44** 1172–9
- Beattie B J, Pentlow K S, Finn R D and Larson S M 2001 A method for the removal of spurious activity in PET imaging introduced by cascade gamma rays *J. Nucl. Med.* **42** 201
- Bergström M, Eriksson L, Bohm C, Blomqvist G and Litton J 1983 Corrections for scattered radiation in a ring detector positron camera by integral transformation of the projections *J. Comput. Assist. Tomogr.* **7** 42–50
- Beshara S, Lundqvist H, Sundin J, Lubberink M, Tolmachev V, Valind S, Antoni G, Långström B and Danielson B G 1999 Kinetic analysis and red cell utilization of  $^{52}\text{Fe}/^{59}\text{Fe}$ -labeled iron (III) hydroxide-sucrose complex following intravenous administration using positron emission tomography *Br. J. Haematol.* **104** 296–302
- Brix G, Zaers J, Adam L E, Bellemann M E, Ostertag H, Trojan H, Haberkorn U, Doll J, Oberdorfer F and Lorenz W J 1997 Performance evaluation of a whole-body PET scanner using the NEMA protocol *J. Nucl. Med.* **38** 1614–23
- Chu S Y F, Ekström L P and Firestone R B 1999 WWW *Table of Radioactive Isotopes* database version 2/28/99 from URL <http://nucleardata.nuclear.lu.se/toi/>
- Flower M A, Al-Saadi A, Harmer C L, McCreedy V R and Ott R J 1994 Dose-response study on thyrotoxic patients undergoing positron emission tomography and radioiodine therapy *Eur. J. Nucl. Med.* **21** 531–6
- Geworski L, Knoop B O, Levi de Cabrejas M, Knapp W H and Munz D L 2000 Recovery correction for quantitation in positron emission tomography: a feasibility study *Eur. J. Nucl. Med.* **27** 161–9
- Graham M C, Pentlow K S, Mawlawi O, Finn R D, Daghighian F and Larson S M 1997 An investigation of the physical characteristics of  $^{66}\text{Ga}$  as an isotope for PET imaging and quantitation *Med. Phys.* **24** 317–26
- Herzog H, Rösch F, Stocklin G, Lueders C, Qaim S M and Feinendegen L E 1993 Measurement of pharmacokinetics of yttrium-86 radiopharmaceuticals with PET and radiation dose calculation of analogous yttrium-90 radiotherapeutics *J. Nucl. Med.* **34** 2222–6
- Herzog H, Tellmann L, Qaim S M, Spellerberg S, Schmid A and Coenen H H 2002 PET quantitation and imaging of the non-pure positron emitting iodine isotope  $^{124}\text{I}$  *Appl. Radiat. Isot.* **56** 673–9
- Karp J S *et al* 1991 Performance standards in positron emission tomography *J. Nucl. Med.* **12** 2342–50
- Kohlmyer S G, Miyaoka R S, Shoner S C, Lewellen T K and Eary J F 1999 Quantitative accuracy of PET imaging with yttrium-86 *J. Nucl. Med.* **40** 280
- Lövqvist A, Lundqvist H, Lubberink M, Tolmachev V, Carlsson J and Sundin A 1999 Kinetics of  $^{76}\text{Br}$ -labeled anti-CEA antibodies in pigs; aspects of dosimetry and PET imaging properties *Med. Phys.* **26** 249–58
- Lubberink M, Janssen F, Schneider H, Bergström M and Lundqvist H 1999 Correction for gamma radiation from non-pure positron emitters in positron emission tomography *Future Directions in Nuclear Medicine Physics and Engineering (Chicago, 21–23 March 1999)* (Chicago: The University of Chicago)
- Lubberink M, Tolmachev V, Widström C, Bruskin A, Lundqvist H and Westlin J E 2002  $^{110\text{m}}\text{In}$ -DTPA-D-Phe<sup>1</sup>-octreotide for imaging of neuroendocrine tumors with positron emission tomography *J. Nucl. Med.* **43** (10)
- Lundqvist H, Lubberink M, Tolmachev V, Lövqvist A, Sundin A, Beshara S, Bruskin A, Carlsson J and Westlin J E 1999 Positron emission tomography and radioimmunotargeting—general aspects *Acta Oncol.* **38** 335–41
- Martin C C, Christian B T, Satter M R, Nickerson L D H and Nickles R J 1995 Quantitative PET with positron emitters that emit prompt gamma rays *IEEE Trans. Med. Imag.* **14** 681–7
- Pentlow K S, Graham M C, Lambrecht R M, Cheung N K V and Larson S M 1991 Quantitative imaging of I-124 using positron emission tomography with applications to radioimmunodiagnosis and radioimmunotherapy *Med. Phys.* **18** 357–66
- Pentlow K S, Finn R D, Larson S M, Erdi Y E and Humm J L 1999 Effects of cascade gamma rays in PET imaging and quantitation *J. Nucl. Med.* **40** 280
- Pentlow K S, Finn R D, Larson S M, Erdi Y E, Beattie B J and Humm J L 2000 Quantitative imaging of yttrium-86 with PET: the occurrence and correction of anomalous apparent activity in high density regions *Clin. Posit. Imag.* **3** 85–90

- Ribeiro M J, Almeida P, Strul D, Ferreira N, Loc'h C, Brulon V, Trebossen R, Maziere B and Bendriem B 1999 Comparison of fluorine-18 and bromine-76 imaging in positron emission tomography *Eur. J. Nucl. Med.* **26** 758–66
- Ribeiro M J, Remy P, Loc'h C, Brulon V and Trebossen R 1999 The influence of positron range on the measurement of a physiopathological antero-posterior gradient in PET imaging of the putamen *Eur. J. Nucl. Med.* **27** 1190
- Rösch F, Blessing G, Linse K H, Herzog H and Qaim S M 1996 Production of the positron emitting strontium isotope Sr-83 and PET phantom measurements preparatory to the evaluation of Sr-89 pharmacokinetics and dosimetry *J. Nucl. Med.* **37** 166
- Rota Kops E, Herzog H, Schmid A, Holte S and Feinendegen L E 1990 Performance characteristics of an eight-ring whole body PET scanner *J. Comput. Assist. Tomogr.* **14** 437–45
- Watson C C, Newport D, Casey M E, DeKemp R A, Beanlands R S and Schmand M 1997 Evaluation of simulation-based scatter correction for 3D PET cardiac imaging *IEEE Trans. Nucl. Sci.* **44** 90–7